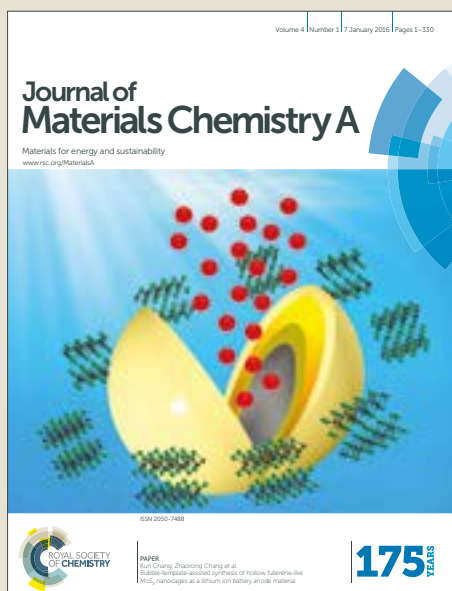


Journal of Materials Chemistry A

Accepted Manuscript



This article can be cited before page numbers have been issued, to do this please use: M. Manzoli, A. Jouve, A. M. Gill, G. Cravotto and R. Raja, *J. Mater. Chem. A*, 2018, DOI: 10.1039/C8TA03656J.



This is an Accepted Manuscript, which has been through the Royal Society of Chemistry peer review process and has been accepted for publication.

Accepted Manuscripts are published online shortly after acceptance, before technical editing, formatting and proof reading. Using this free service, authors can make their results available to the community, in citable form, before we publish the edited article. We will replace this Accepted Manuscript with the edited and formatted Advance Article as soon as it is available.

You can find more information about Accepted Manuscripts in the [author guidelines](#).

Please note that technical editing may introduce minor changes to the text and/or graphics, which may alter content. The journal's standard [Terms & Conditions](#) and the ethical guidelines, outlined in our [author and reviewer resource centre](#), still apply. In no event shall the Royal Society of Chemistry be held responsible for any errors or omissions in this Accepted Manuscript or any consequences arising from the use of any information it contains.



Spectroscopic insights leading to a better understanding of site-isolation in heterogeneous nanocatalysts

Maela Manzoli,^{*a} Andrea Jouve,^b Arran M. Gill,^c Giancarlo Cravotto,^a and Robert Raja^c

Received 00th January 20xx,
Accepted 00th January 20xx

DOI: 10.1039/x0xx00000x

www.rsc.org/

Pt nanoparticles (NPs) extruded from a copper chloropyrophosphate (CuCIP) framework have been synthesized with different metal loadings and evaluated in the KA oil oxidation with molecular oxygen. Before reaction, the catalysts were subjected to an activation procedure in reducing atmosphere at 200 °C in order to extrude the Pt NPs. Having an optimal loading of active sites (Pt nanoparticles) leads to superior turnover frequencies and a combined structural and spectroscopic approach was used to probe the nature of the extruded nanoparticle catalysts. For the first time, we were able to track the extrusion and NP formation through the use of PXRD and DR UV-vis-NIR spectroscopy, monitoring the effective inclusion of [PtCl₄]²⁻ anions from the metal precursor within the 1D channels of the framework, during the synthesis and associated extrusion process. A direct correlation between the degree of extrusion and catalytic performance has been proposed and the importance of site-isolation in achieving high catalytic turnovers has been emphasized, on the basis of the spectroscopic analysis that has been carried out. HR-TEM analysis showed the presence of homogeneous and highly dispersed Pt NPs, which further illustrated the structural and compositional integrity of the supported nanoparticles, post catalysis. Interestingly, a narrower particle size distribution at optimal metal loadings (3 wt% Pt) was found, further vindicating the importance of designing uniformly-distributed metal nanoparticles for continuous-flow oxidation processes. Furthermore, our investigations on NP-substrate interactions through probe-based *in situ* FT-IR studies, provides unique insights on the catalytic reaction, by precisely tracking the main steps involved in the oxidation process. Cyclohexanol molecules interact with the catalyst through the OH group without decomposing until 150 °C, and its subsequent oxidation to cyclohexanone is evidenced at 200 °C."

Introduction

Since the commercial process for nylon 6,6 production was implemented in 1939, polyamide resins have become of huge interest for the plastics industry. Cyclohexanone is now a vital commodity chemical within the industry with approx. 3 million tonnes produced per year for the production of both adipic acid, via oxidation, and ϵ -caprolactam via oximation followed by the Beckmann rearrangement, essential precursors in the industrial manufacture of nylon 6,6 and nylon 6 respectively.¹⁻⁴ There exists three primary industrial routes towards synthesizing a cyclohexanone product: the hydrogenation of phenol, the direct oxidation of cyclohexane and the dehydrogenation of cyclohexanol.

Associated advantages and disadvantages depend on the process for which the product is required as optimum feedstock purity and/or cyclohexanone to cyclohexanol ratios required, differ for both adipic acid and ϵ -caprolactam. For adipic acid a mixture of cyclohexanone and cyclohexanol (KA oil) is desired as opposed to the very high purity

cyclohexanone product that is required for the production of ϵ -caprolactam. The high quality of the cyclohexanone product required is a result of its position in the early stages of the process towards the synthesis of nylon 6. Impurities in the initial feedstock would be detrimental to the caprolactam polymerization as well as effecting the final properties of the polyamide, such as its colouration and ageing resistance.⁵

All three processes for cyclohexanone production suffer from contaminated products, with phenol and cyclopent-1-ene-1-carbaldehyde (cyclohexane oxidation) causing significant problems from a purification perspective. Both compounds are difficult to purify through distillation, more so phenol due to its azeotropic mixtures with both cyclohexanol and cyclohexanone, whereas cyclopent-1-ene-1-carbaldehyde also responds to a number of cyclohexanone qualification tests, particularly those commonly used for ϵ -caprolactam feedstocks e.g. UV and oxidation tests.⁶⁻⁹

We propose the aerobic oxidation of the existing KA oil feedstock as a viable alternative due to its high atom economy (approx. 85 %), yields and purity of product as well as its minimal need for high specific investment due to utilization of an existing feedstock and lack of additional purification processes or co-catalysts/additives.¹⁰

Due to its significance, investigations into the production of cyclohexanone from cyclohexanol have been extensive (see

^a Department of Drug Science and Technology and NIS Interdepartmental Centre, University of Torino, 10125 Torino, Italy. *Email - maela.manzoli@unito.it

^b Department of Chemistry, University of Milano, 20133 Milano, Italy.

^c School of Chemistry, University of Southampton, Southampton SO17 1BJ, UK.

† Electronic Supplementary Information (ESI) available: Tables SI-1 and SI-2, and Figures S1-S10. See DOI: 10.1039/x0xx00000x

Table SI-1). While this is true the majority of these employ a dehydrogenation pathway and although alcohol conversions and ketone selectivities are good (both typically >80 %) these methods require notoriously high temperatures of >300 °C.¹¹⁻¹⁴ Oxidation processes have commonly used peroxides due to the higher levels of ketone selectivity (>90%) and lower temperatures they can attain. However, despite the advantages, these generally require solvents, typically employ batch systems and often suffer from lower conversions (<50 %), not to mention the toxic/corrosive nature of the oxidant.¹⁵⁻¹⁸

Therefore a more sustainable approach would be to utilize molecular oxygen or air as the oxidant. On top of the added environmental factors these aerobic and O₂ based processes are more suitable for continuous-flow approaches and generally deliver very high levels of selectivity (>90 %).¹⁹⁻²⁴ Despite the aforementioned advantages many of these aerobic and molecular oxygen systems utilize a batch process which often require additives and/or solvents. Hence one can foresee the catalytic potential of an aerobic based system, specifically if a continuous-flow process can be employed as this would remove the issue of catalyst separation, facilitate greater control of residence times and improve industrial scale safety.²⁵

Despite some impressive catalytic performances being reported and on top of the drawbacks mentioned, nearly all research into catalytic cyclohexanone production employs a pure cyclohexanol feedstock, requiring the demanding separation of KA oil or the costly capital investment required to utilize the pure alcohol feedstock, as highlighted. Therefore, there is huge incentive to develop catalytic systems that are more diverse and able to utilize KA oil and air directly as much more sustainable feedstocks.

The benefits of using supported metal nanoparticles (NPs) has afforded numerous advantages, as creating uniformly distributed active sites on a high-surface area support, greatly enhances the stability and lifetime of these materials in industrially-significant catalytic processes.²⁶⁻³¹ With this in mind, microporous transition metal phosphates present as a chemically flexible alternative to more traditional open-framework supports. It has been shown³²⁻³³ that the incorporation of fluoride and chloride ions into copper phosphates improves their stability while allowing for intricate ion exchange properties to be exploited. It is the combination of the halide ions and the low charge density of the Cu^{II}, *d*⁹ centres that facilitates the considerable degree of ionic mobility within these systems, particularly for copper chloropyrophosphate (CuCIP) structures.³⁴⁻³⁵

These open-framework CuCIP materials consist of μ⁴ chloride ions at the apex of 4 × CuO₄Cl square-based pyramids. Pyrophosphate (P₂O₇) units link these quartets forming 1D channels approx. 12.7 Å in diameter. The channels are occupied by charge compensating Rb⁺ cations and tetrachloro metallate anions such as [CuCl₄]²⁻, [AuCl₄]⁻, [PdCl₄]²⁻ or [PtCl₄]²⁻.^{35,36}

Incorporation of these tetrachloro metallate ions gives these materials exceptional potential from a catalytic perspective

affording a facile route toward generating supported, uncapped, small metallic NPs via a novel extrusion method.

The extrusion of the [MCl₄]^{x-} moieties occurs via a reduction protocol, whereby the system is subjected to elevated temperatures under a H₂ flow. This process causes the extrusion of the metallic species towards the materials surface resulting in homogeneously distributed metallic nanoparticles, liberating HCl and the RbCl by-product in the process in order to maintain the neutrality of the host framework.

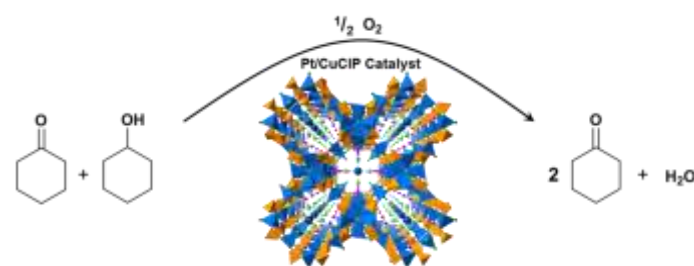
Therefore the idea of constructing hybrid materials that facilitate the controlled formation of active metallic NP centres supported on a chemically diverse porous phosphate material, could prove to be an effective strategy from a catalytic stand point. Indeed the M/CuCIP (M = Au, Pt & Pd) materials have already demonstrated high levels of catalytic activity in a range of industrially-significant, selective alcohol oxidations: benzyl,^{36,37} vanillyl³⁸ and more recently, KA oil.³⁹

In this work we showed Pt NPs of 2-5 nm diameter, extruded from a CuCIP framework catalytically outperformed (according to Scheme 1) their Au and Pd counterparts by an order of magnitude.^{38,39} Complementary *ex situ* analysis through X-ray photoelectron (XPS) and X-ray adsorption spectroscopic methods showed the crucial role of the activation protocol on the catalytic activity of these materials, accurately demonstrating the progression from Pt^{II} to Pt⁰ as a function of temperature under a hydrogen atmosphere (150-200 °C for 2 hr under a 5% H₂/N₂ flow).³⁹

Indeed, through the use of these activated Pt/CuCIP NP catalysts some of us have been able to produce cyclohexanone utilizing a continuous-flow system, under aerobic conditions, with unrivalled yields of upwards of 90%, overcoming all of the aforementioned hindrances to the previously investigated catalytic systems.⁴⁰

Here we report the manipulation of the Pt loading and its impacts on both the host framework and ensuing catalysis, post-extrusion. For the first time we are able to track the extrusion and NP formation through the use of PXRD and DR UV-vis-NIR demonstrating the control over NP size afforded by these systems. Furthermore, we investigate the NP-substrate interactions through probe molecule FT-IR studies directly observing the oxidation transformation. Thus we aim to optimise the catalytic performance via adroit catalyst design, while enhancing our understanding of the catalyst-substrate interface.

Scheme 1 KA oil selective oxidation to cyclohexanone with molecular O₂ over the 7 wt. % Pt/CuCIP catalyst.



Experimental

Materials

Hydrothermal synthesis of Pt-containing copper chloropyrophosphate frameworks with different metal loading. The Pt-containing copper chloropyrophosphate framework synthesized formula is $[\text{Rb}_9\text{Cu}_6(\text{P}_2\text{O}_7)_4\text{Cl}]\cdot[\text{PtCl}_4]\text{Cl}_2$. Copper(II) fluoride (0.1168 g, 1.150 mmol), 85 wt. % orthophosphoric acid (0.2 mL, 2.922 mmol), 50 wt. % rubidium hydroxide (0.24 mL, 2.037 mmol), rubidium chloride (0.28 g, 2.316 mmol) and potassium tetrachloroplatinate (0.0515 g, 0.124 mmol) were mixed in the Teflon® liner of a custom-made 23 mL hydrothermal vessel. The vessel was sealed and heated within a fan assisted oven to 175 °C for 48 hr. After which the materials were filtered and washed with 250 mL of deionized water and dried before activation. The obtained materials are: 1 wt. % Pt/CuClP, 3 wt. % Pt/CuClP, 5 wt. % Pt/CuClP, 7 wt. % Pt/CuClP. The blank framework was also investigated as a reference sample. The fresh materials appear as brilliant green cubic crystals. All chemicals were purchased from Sigma Aldrich and Fisher Scientific and used without further purification.

Thermal activation procedures. The samples were then activated under reductant conditions: under a flow of 5% H_2/N_2 at approx. 150 mLmin^{-1} , for 2 hr at 200 °C. After reduction, the Pt catalyst showed a darker khaki-green colour. A digital image taken on the catalysts with different Pt loading after activation are reported in Figure SI-1. The samples display progressively darker colour with the increase of the Pt content. Gases were sourced from BOC Industrial Gases and used as supplied.

Methods

Catalytic tests. Catalytic reactions were carried out in a fixed-bed flow reactor using 0.20-0.25 g pelletized catalyst. The system was set up and purged under air flow at 200 °C for 1 hr before the substrate feed was allowed to saturate the system. The substrate and air flow rates were set to their experimental level and left to equilibrate (reaching a steady state) for 1 hr. The reactions were carried out using an air flow of 25 mLmin^{-1} , a substrate flow of 15 μLmin^{-1} and at 200 °C unless stated otherwise.

KA oil solutions were made up as a 1:1 weight ratio of cyclohexanol and cyclohexanone and used as the substrate feedstock. An external standard solution of triethylene glycol dimethyl ether (2 M) in acetone was fed into the off stream of the reactor at the same rate of flow as the substrate. The solution obtained from the off stream was diluted at a ratio of 1:10 with acetone before being subject to GC analysis (PerkinElmer, Clarus 480) using an Elite-5 column equipped with a flame ionization detector. Products were identified against authenticated standard and quantified by calibration to obtain response factors against the known external standard. The turn over frequency (TOF) was calculated via the relationship below and the turn over number (TON) was calculated as the sum of the individual TOFs over 18 hr of reaction:

$$\text{TOF} = \frac{\text{Cyclohexanol Conversion (mol min}^{-1}\text{)}}{\text{Catalyst Metal Content (mol)}} \times \text{Sample Time (60 min)} \\ = [\text{hr}^{-1}]$$

Characterisation of the catalysts. Powder X-Ray Diffraction (PXRD) measurements were performed on a Bruker D2 Phaser diffractometer using $\text{Cu K}\alpha_1$ radiation ($\lambda = 1.5406 \text{ \AA}$).

Diffuse reflectance UV-Vis-NIR analysis was carried out on the samples in the form of powders. The samples were placed in a quartz cell, allowing treatments in controlled atmosphere and temperature, but spectra were only recorded at room temperature (r.t.).

Diffuse reflectance UV-Vis-NIR spectra were run on a Varian Cary 5000 spectrophotometer, working in the range of wavenumbers 190-2500 nm. UV-Vis-NIR spectra are reported in the Kubelka-Munk (K-M) function:

$$F(R_\infty) = \frac{(1 - R_\infty)^2}{2R_\infty} = \frac{K}{s}$$

where R_∞ is the reflectance of an "infinitely thick" layer of the sample, K is the molar absorption coefficient and s is the scattering coefficient. $F(R_\infty)$ is usually termed the remission or K-M function. All spectra were acquired in air and the samples were examined without any preliminary activation.

Transmission electron microscopy (TEM) and high resolution (HR-) TEM measurements were performed using a side entry Jeol JEM 3010 (300 kV) microscope equipped with a LaB_6 filament and fitted with X-ray EDS analysis by a Link ISIS 200 detector. For analyses, the powdered samples were deposited on a copper grid, coated with a porous carbon film. All digital micrographs were acquired with an Ultrascan 1000 camera and the images were processed by Gatan digital micrograph. For each sample, a representative number of images was acquired and the Fourier Transformed (FT) of the images were analysed. Moreover, a statistical evaluation of the size of the Pt particles was performed for each material. Histograms of the particle size distribution were obtained by considering at least 300 particles on the HRTEM images, and the mean particle diameter (d_m) was calculated as:

$$d_m = \frac{\sum d_i n_i}{\sum n_i}$$

where n_i was the number of particles of diameter d_i . The counting was carried out on electron micrographs acquired starting from 150,000 magnification, where Pt nanoparticles contrasted with respect to the CuClP framework were detected.

The metal specific surface area (SSA) was also calculated based on the TEM and HR-TEM for the fresh, activated and used samples. A spherical shape of all exposed Pt NPs was assumed and the following formula was applied:

$$\text{SSA} = 3 \sum \frac{n_i r_i^2}{(\rho_{\text{Pt}} \times \sum n_i r_i^3)} = [\text{m}^2 \text{g}^{-1}]$$

where r_i is the mean radius of the size class containing n_i particles, and ρ_{Pt} the volumetric mass of Pt (21.45 g/cm^3).

The FTIR spectra were collected on a Perkin-Elmer 2000 spectrometer (equipped with MCT detector) with the samples in self-supporting pellets (approx. 0.17 g) introduced in cells allowing thermal treatments in controlled atmosphere and spectrum

scanning at r.t. and at $-180\text{ }^{\circ}\text{C}$. In addition, a stainless steel AABSPEC 2000 cell allowing to run the spectra *in situ* in controlled atmosphere and temperature was also employed to monitor the reaction spectroscopically under catalysis conditions. From each spectrum, the spectrum of the sample before the inlet of the reactant molecule was subtracted. Before the FTIR experiments, the samples were previously activated to remove water and carbonate-like species, due to air exposure, and to make the sites available to the reactants. The steps of reductive thermal treatment are summarized in Table 1.

Results and Discussion

Structural analysis of the fresh, activated and post catalysis Pt/CuClIP materials

PXRD measurements were performed on all the fresh, activated (i.e. reduced at $200\text{ }^{\circ}\text{C}$ for 2 hr in 5% H_2/N_2 flow) and used materials (after 4-6 hr reaction) with different Pt loadings and the results are shown in Figure 1.

The structural stability of these materials was confirmed by the PXRD measurements, in which no significant differences among the peaks related to the CuClIP framework were observed, demonstrating the stability of this catalytic material from a structural point of view both before and after reaction (Figure SI-2). This is further supported by the un-doped framework showing no changes under analogous conditions (Figure SI-3), suggesting that any changes observed are directly due to the incorporation of the $[\text{PtCl}_4]^{2-}$ ions and the ensuing extrusion process. With the exception of the PXRD pattern of the activated 1 wt. % Pt/CuClIP catalyst, that is indistinguishable from the un-activated sample due to reasons discussed later in this article, close inspection of the PXRD patterns (Figure 1) indicate that the peaks at 2θ 15.5° , 25.5° , 36.5° and 44.8° (wine bars) display maximum intensity in the fresh catalysts (Figure 1a). Then such peaks decrease during reduction to a point where they are no longer visible after activation (Figure 1b) and are unaffected by catalysis (Figure SI-2). It is also apparent that these peaks dramatically increase in intensity with increasing Pt loading and are not present within the PXRD pattern of the un-doped framework (Figure 1a).

Therefore we hypothesise that these reflections are from the Pt containing crystallographic planes, possibly due to the $[\text{PtCl}_4]^{2-}$ units ordered within the CuClIP channels, explaining their depreciation upon extrusion and removal of the Pt species from the framework channels. This is further evidenced by the emergence of both metallic Pt and RbCl phases (Figure 1b, black and blue bars, respectively). Both phases are a direct result of the extrusion process and follow the reverse trend to that observed above for the Pt containing CuClIP crystallographic planes.

Table 1 Steps involved in the reductive thermal treatment.

Step	Description
1	r.t. \rightarrow $150\text{--}200\text{ }^{\circ}\text{C}$, $P < 1 \cdot 10^{-5}$ mbar
2	3 inlets of 10 mbar H_2 at $150\text{--}200\text{ }^{\circ}\text{C}$ (10 min each one) – vacuum
3	$150\text{--}200\text{ }^{\circ}\text{C} \rightarrow$ r.t. under outgassing

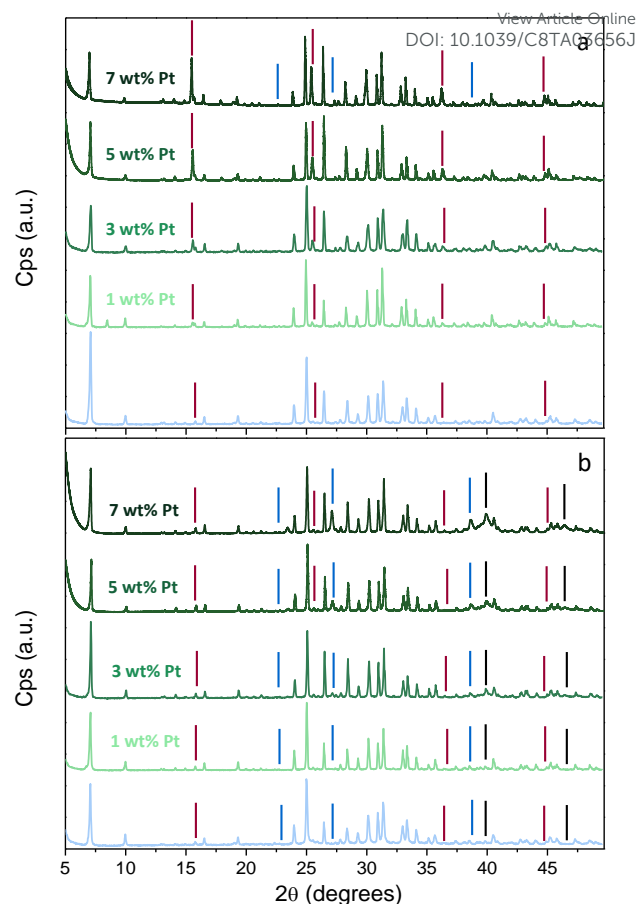


Fig. 1 PXRD patterns of all percentage loading of Pt in fresh (a) and activated at $200\text{ }^{\circ}\text{C}$ (b) Pt/CuClIP materials (green curves), and blank framework (light blue curves). The peaks assigned to Pt containing crystallographic planes (wine bars), RbCl (blue bars) and metallic Pt (black bars) phases are indicated.

The metallic Pt reflections present at 39.6° and at 46.3° , assigned to the (111) and (200) planes respectively (see Figure 1b, black bars and Figure SI-2), both with broad signals suggesting the presence of small crystallites or NPs. Similarly the RbCl reflections at 23.3° , 27.1° and 38.7° represent the (111), (002) and (022) planes respectively (blue bars and Figures SI-2 and SI-4). These show increasing intensity with Pt loading after activation (Figure 1b). This is a consequence of the removal of Rb^+ ions from the framework in order to maintain an overall neutral charge through decomposition of the $[\text{PtCl}_4]^{2-}$ species. These observations are also consistent with previous XPS analysis carried out on the high loading 7 wt. % Pt/CuClIP materials which showed the progression of Pt^{II} to Pt^0 on the material surface with an increase in activation temperature.³⁹ These observations would then demonstrate the ability to track the removal of $[\text{PtCl}_4]^{2-}$ species from the framework channels and the concurrent metallic Pt NP formation across a variety of metal loadings. Interestingly, depending on the Pt content, the peaks related to the presence of metallic Pt and RbCl display a different behaviour (Figure SI-2). In particular, no changes were observed in the pattern of the 1 wt. % used catalyst, seeming to indicate that no crystalline Pt NPs were extruded, at very low Pt loadings. Further, no significant changes in intensity were observed for the 3, 5 or 7

wt. % Pt catalyst after 6 hrs reaction, pointing out that the extrusion process was complete after activation at 200 °C. These differences may possibly arise either from the presence of the Cu chloride anions within the 1D channels hampering the Pt chloride anions extrusion. Therefore, we have been able to describe the efficiency of the extrusion process directly through the use of PXRD while also affording insights into the exact nature of the process and the production of the RbCl phase.

The fresh, activated and used catalysts with different Pt loadings (1, 3, 5 and 7 wt. %) were investigated by DRUV-Vis spectroscopy. The spectra of the fresh samples are compared in Figure 2. As already discussed, the samples are green coloured, displaying different colour gradation dependant on both activation (see Figure SI-1) and Pt loading. In all cases, very complex spectra were obtained and explained for the first time. Bands at 41500, 35300 and 27000 cm^{-1} , here assigned to metal ligand charge transfer (CT) between Cu^{II} and Cl atoms belonging to the $[\text{CuCl}_4]^{2-}$ ions in the framework are observed (Figure 2).⁴¹ In addition, the broad and complex absorptions at low energy are involving the d-d electronic transitions of Cu^{II} species. More in detail, the band at 11850 cm^{-1} can be ascribed to the d-d transition of the $[\text{CuCl}_4]^{2-}$ ions where the Cu^{II} exhibits a square planar configuration (D_{4h} symmetry).⁴¹ These species are embedded within the 1D channels of the framework. The component at 9900 cm^{-1} is possibly due to the Cu d-d transition of tetrahedral $\text{Cu}^{\text{II}}\text{O}_4$ species where the Cl^- ions are located at the apex of CuO_4Cl square-based pyramids of the framework.⁴¹ The absorptions decrease in intensity with the amount of Pt precursor (see also Figure SI-5), whilst a component at 22000 cm^{-1} becomes more pronounced when the Pt loading is increased (inset of Figure 2). This absorption is related to the CT $\text{Pt}^{\text{II}}\text{-Cl}$ of the square planar $[\text{PtCl}_4]^{2-}$ units.⁴² It is therefore suggested that its increase in intensity is a result of the increased amount of metal precursor inserted during the synthesis and it can be due to the presence of $[\text{PtCl}_4]^{2-}$ moieties, supporting the proposed mechanism of incorporation depicted in Scheme 2.

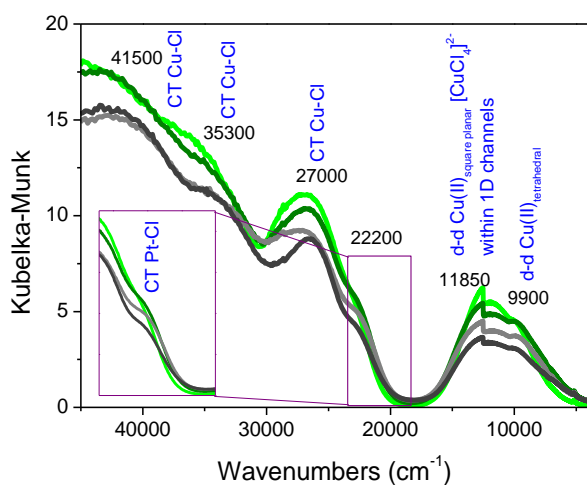
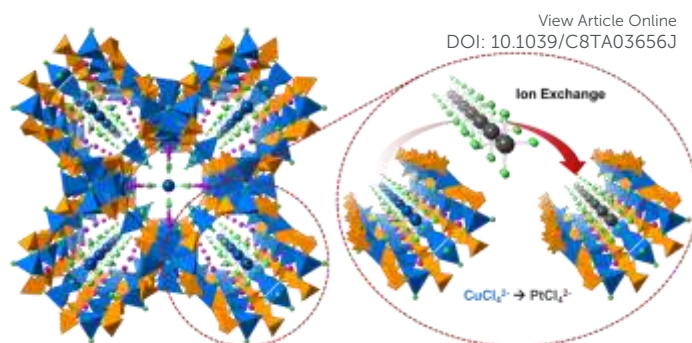


Fig. 2 DRUV-Vis spectra of 1 wt. % Pt/CuClIP (green curve), 3 wt. % Pt/CuClIP (dark green curve), 5 wt. % Pt/CuClIP (grey curve) and 7 wt. % Pt/CuClIP (dark grey curve). Inset: zoom of the spectra in the 26000-17550 cm^{-1} range.



Scheme 2 Graphical illustration outlining the insertion of the Pt precursor in the 1D channels of the CuClIP framework via an ion-exchange method. Left: crystal structure of the $[\text{Rb}_9\text{Cu}_6(\text{P}_2\text{O}_7)_4\text{Cl}].[\text{PtCl}_4]\text{Cl}_2$ framework (Pt – grey, Cl – green, Rb pink, Cu – blue, P – orange and oxygen has been omitted for clarity).

To have more insights on the evolution of the catalyst upon activation and after catalysis, the comparison among the DRUV-Vis spectra of the fresh (green curve), activated (ochre curve) and used (dark grey curve) 1 wt. % Pt/CuClIP sample is shown in Figure 3. If compared to the fresh material (green curve), the activation procedure (ochre curve) provoked a decrease in intensity of the absorptions at 41500, 35300 and 27000 cm^{-1} , due to the $\text{Cu}^{\text{II}}\text{-Cl}$ CT, whereas the absorptions involving the d-d electronic transitions of Cu species seemed not to vary significantly. At the same time, although weaker, the component due to the Pt precursor species is still detected at 22200 cm^{-1} , pointing out the enhanced sensitivity of DR UV-Vis over PXRD which revealed no deviation in the pattern for the low loading 1 wt. % Pt sample. Upon activation at 200°C, the intensity of such absorption decreases with increasing Pt content (see Figures 4a and 4b), giving evidence that the extrusion of Pt NPs increases with the Pt loading after the reduction process, in agreement with PXRD findings.

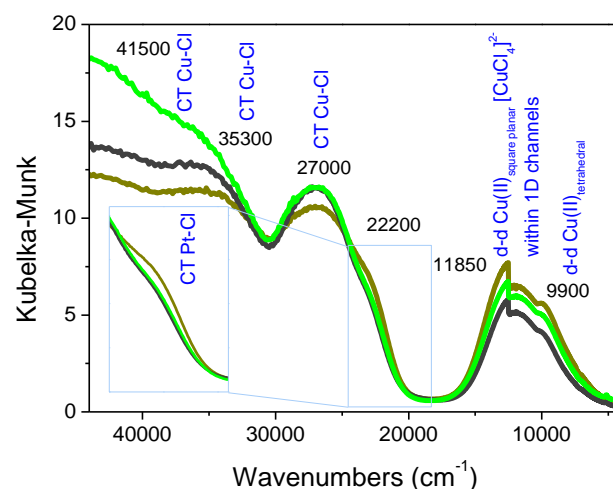


Fig. 3 DRUV-Vis spectra of the fresh (green curve), activated (ochre curve) and used (dark grey curve) 1 wt. % Pt/CuClIP catalyst. Inset: zoom of the spectra in the 25000-19500 cm^{-1} range.

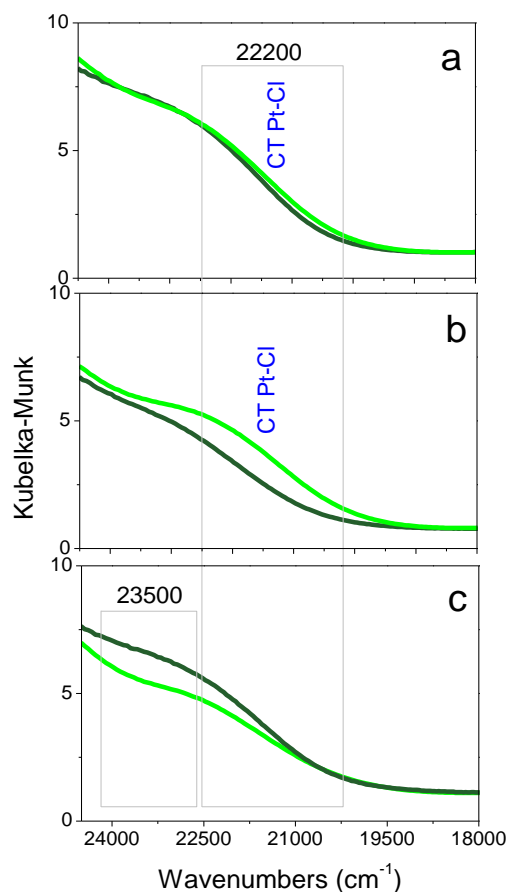


Fig. 4 DRUV-Vis spectra of the fresh (green curve), activated (dark green curve) of 3 wt. % Pt/CuClIP (section a), 5 wt. % Pt/CuClIP (section b) and 7 wt. % Pt/CuClIP (section c) catalysts. Inset: zoom of the spectra in the 24500-18000 cm^{-1} range.

Moreover, a new component at 23500 cm^{-1} is observed in the case of the high loading 7 wt. % CuClIP catalyst (Figure 4c). Bands in the 14000-25000 cm^{-1} range were ascribed to the presence of Pt metal NPs with size 2-5 nm.⁴³ Generally, catalyst activation at 200 °C is responsible for a decrease in intensity of the Cu-Cl bands with increasing Pt loading (Figure SI-5). This feature further corroborates that the $[\text{CuCl}_4]^{2-}$ moieties are located within the 1D channels and prevent the extrusion process at lower loadings.

Surface reactivity: in situ study of KA oil oxidation

In order to probe the cyclohexanol-Pt interactions liquid cyclohexanol was dropped directly on a pellet of the Pt 7 wt. % catalyst previously activated and then the AABSPEC cell was gradually heated at 200 °C in cyclohexanol atmosphere and the FTIR difference spectra obtained, Figure 5.

Upon interaction with cyclohexanol at room temperature and subsequent heating at 150 °C, a broad band between 3550 and 3200 cm^{-1} , due to the stretching modes of the OH groups of cyclohexanol was observed simultaneously with two sharp and intense peaks at 2930 and 2850 cm^{-1} assigned to the asym and sym C-H stretching modes of cyclohexanol. At lower frequency, weak bands at 1070, 1024, 970 and 880 cm^{-1} assigned to the C-O

bending/stretching modes of the alcohol were also detected. These absorptions are strictly related to the unreacted cyclohexanol and reach the maximum intensity around 150 °C, meaning that until this temperature the alcohol molecule interacts with the catalyst mainly through the OH group without decomposing. These spectroscopic features are also an indication of the efficient activation of the cyclohexanol reactant molecule on the catalyst surface up to 150°C. Subsequently, the intensity of the bands start to decrease as soon as the temperature reaches 200 °C when a peak at 1715 cm^{-1} gets to its maximum intensity (inset in Figure 5). This absorption is related to the C=O stretching mode of cyclohexanone and its intensity progressively grows with time, indicating that at 200°C the oxidation process begins to occur as the cyclohexanol is oxidised to cyclohexanone, which further confirms that 200°C is the optimum temperature for selective oxidation of KA oil. Moreover, no additional bands are observed (and confirmed by separate GC and GC/MS analysis), indicating that the reaction occurs without the formation of any further reaction intermediates. Therefore, the *in situ* spectroscopic analysis precisely tracks the main steps involved in the catalytic reaction: (i) cyclohexanol adsorption and activation, reasonably through the OH group; (ii) oxidation of the OH group to C=O group at 200 °C to produce cyclohexanone. Finally, the bands were easily removed after simply outgassing the sample (residual pressure below 1×10^{-3} mbar), demonstrating that the cyclohexanol/cyclohexanone mixture can be efficiently removed from the catalyst surface after reaction (Figure SI-6) and pointing out the facile removal and cleansing of the catalyst surface and active sites.

Catalytic activity in the KA oil oxidation

Figure 6 contrasts the influence of Pt loading in the Pt/CuClIP catalysts with turnover frequencies (TOFs) and cyclohexanone selectivity for the aerobic oxidation of KA oil.

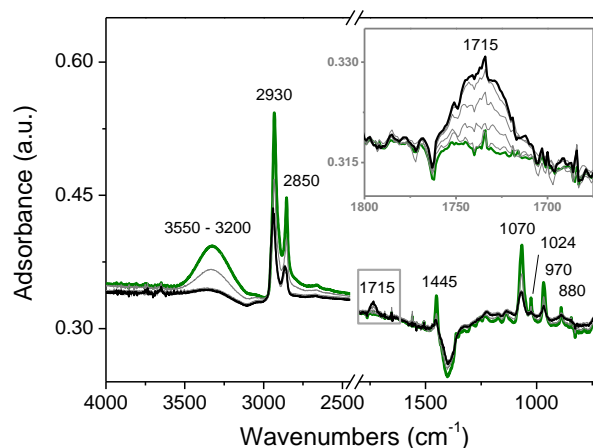


Fig. 5 FTIR difference spectra of the 7 wt. % Pt/CuClIP sample in dropped cyclohexanol at 150 °C (green curve) and at increasing contact times at 200 °C (every 10 min, grey curves) up to 50 min (black line, attainment of equilibrium) at the same constant temperature (200 °C). B. Inset: close view of the same spectra reported in the previous figure to highlight the behaviour of the band at 1715 cm^{-1} , related to the C=O stretching mode of cyclohexanone.

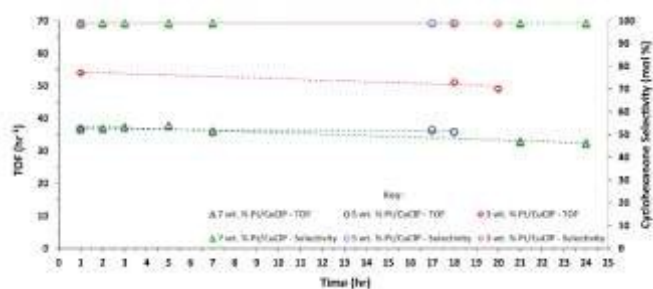


Fig. 6 Time on stream data showing TOF on the left axis (bold colour) and cyclohexanone selectivity on the right axis (pale colour) for the 3 (red), 5 (blue) and 7 (green) wt. % Pt/CuCl₂ catalysts. Note: both the 1 wt. % Pt/CuCl₂ sample and the un-doped framework showed no catalytic activity.

All catalysts display consistently high levels of cyclohexanone selectivity (>99%) and extended catalytic lifetime's, characteristic of these systems.³⁹ Furthermore, there is a clear influence of Pt loading with the observed TOFs; 924, 654 and 514 for the 3, 5 and 7 wt. % Pt/CuCl₂ catalysts respectively. Clearly, the most active and efficient catalyst is the one with the modest metal loading (3 wt%), demonstrating that the lower abundance of metal and resulting enhanced levels of NP site isolation bestow enhanced catalytic performance. The dramatic decrease in TOF between the 3 wt. % sample and the corresponding analogues with higher metal loading further vindicates the industrial applicability from an economic standpoint.

While one would expect even higher rates of turn over at lower metal loadings (1 wt %), the lack of NP extrusion, due to high [CuCl₄]²⁻ content within the channels, as evidenced by the Cu^{II} d-d band at 11850 cm⁻¹ in Figure 3 and (Figure SI-5), restricts Pt NP formation and renders this catalyst inactive. Despite the limitations of this system at low metal loadings, there clearly exists the potential to utilize this unique extrusion process at modest metal loadings, i.e. around 3 wt. % to achieve optimal catalytic activities that result in high TOFs. At these loadings, the extrusion process affords catalytically active and robust NP species, which tend to become catalytically less efficient at progressively higher loadings of 5 and 7 wt. %.

Thus, the degree of extrusion of these NP species, in conjunction with the inherent ion exchange properties of the framework, could facilitate the manipulation of the active site to suit the catalytic requirements, affording accurate control over metal loading as well as NP size and distribution. Given the prominence of the optimal 3 wt. % Pt/CuCl₂ catalyst, in terms of its enhanced TOFs, HR-TEM has been utilized in order to explore the influence of site-isolation.

Controlling site isolation and the impacts of catalysis on the nanoparticle environment

TEM and HR-TEM analyses were carried out on the fresh, activated and used 3 wt. % Pt/CuCl₂ catalyst, in order to ascertain eventual changes in Pt NP size occurring upon activation and/or during catalysis. The results are reported in Figure 7. The TOF are fairly consistent for the entire duration of the catalysis and minimal deactivation was observed with time-on-stream studies over 24 h

(Figure 6). It is interesting to observe Pt spherical NPs, appearing darker with respect to the CuCl₂ framework and with average size of 2.8 ± 1.4 nm, on the fresh catalyst (Figure 6a, highlighted by green arrows), before the reduction process. On this sample, the large majority of the NPs were <3 nm in diameter, as revealed by the particle size distribution reported in section d of the same Figure.

Despite the presence of small NPs upon the materials surface this particular system (fresh, before activation) showed no catalytic activity, implying the very small number of particles, shown to be only located on thin fringes of the sample, are insufficient to produce measurable catalytic activity, similar to the low loading 1 wt. % Pt/CuCl₂ material.³⁹ Demonstrating that thorough surface coverage of the host framework is required in order to achieve an efficient catalytic system. EDS analysis reveals a Pt concentration in agreement with the effective metal loading of the catalyst, 3 wt. % (section c of Figure SI-7), proving good accuracy and optimal inclusion of the metal precursor. It should also be noted that a very small percentage of K⁺ is incorporated from the K₂PtCl₄ salt precursor.

It is known that the parent framework can form analogously with both Rb⁺ and K⁺ ions, further demonstrating the innate flexible ion exchange properties in play.¹⁰ As expected, a much larger number of Pt NPs, homogeneously distributed upon the framework, is observed on the activated sample if compared to the fresh material (Figure 6, section b). The average size is 3.6 ± 1.1 nm and the particle size distribution reveals that almost the totality of the NPs have size in the 3-5 nm range (see section e) and the EDS analysis confirms no platinum is lost upon activation or post-catalysis (section e of Figure SI-8). Moreover, the framework was not damaged upon the reduction process, as revealed by the persistent presence of diffraction fringes typical of the CuCl₂ framework, in agreement with the PXRD discussed previously.

Interestingly, a decrease of chlorine content in the activated and used samples was observed with respect to that of the fresh material (from 10.01 to 0.49 and 1.25 atomic %, see Figure SI-9). Such a feature could be attributed to the reduction of the metal precursor: it is assumed that during the reducing process the [PtCl₄]²⁻ moieties release Cl in the form of HCl gas (as well as RbCl). Moreover, the d-spacing obtained for the crystalline structure of the CuCl₂ framework are listed in Table SI-2 and are comparable with those reported in the paper by Hinde *et al.*³⁹ An agglomeration of the NPs with size of 3 nm into NPs with size of 5 nm occurred during the catalysis and this is evident looking at Figure 6c and at the particle size distribution reported in section f. The Pt NP size distribution is broader, indeed some particles of about 10 nm are also observed. An average particle size of 4.8 ± 1.7 nm was found. Moreover, the sample has maintained its crystallinity confirming its high resistance under catalytic conditions, as confirmed by the measured d-spacing's (Figure SI-10) in agreement with PXRD results.³⁹ To rule out the influence of particle size effect on the catalytic activity, additional HR-TEM measurements were performed on the high loading 7 wt. % Pt/CuCl₂ catalyst upon activation and post-catalysis (Figure 8a and 8b, respectively).

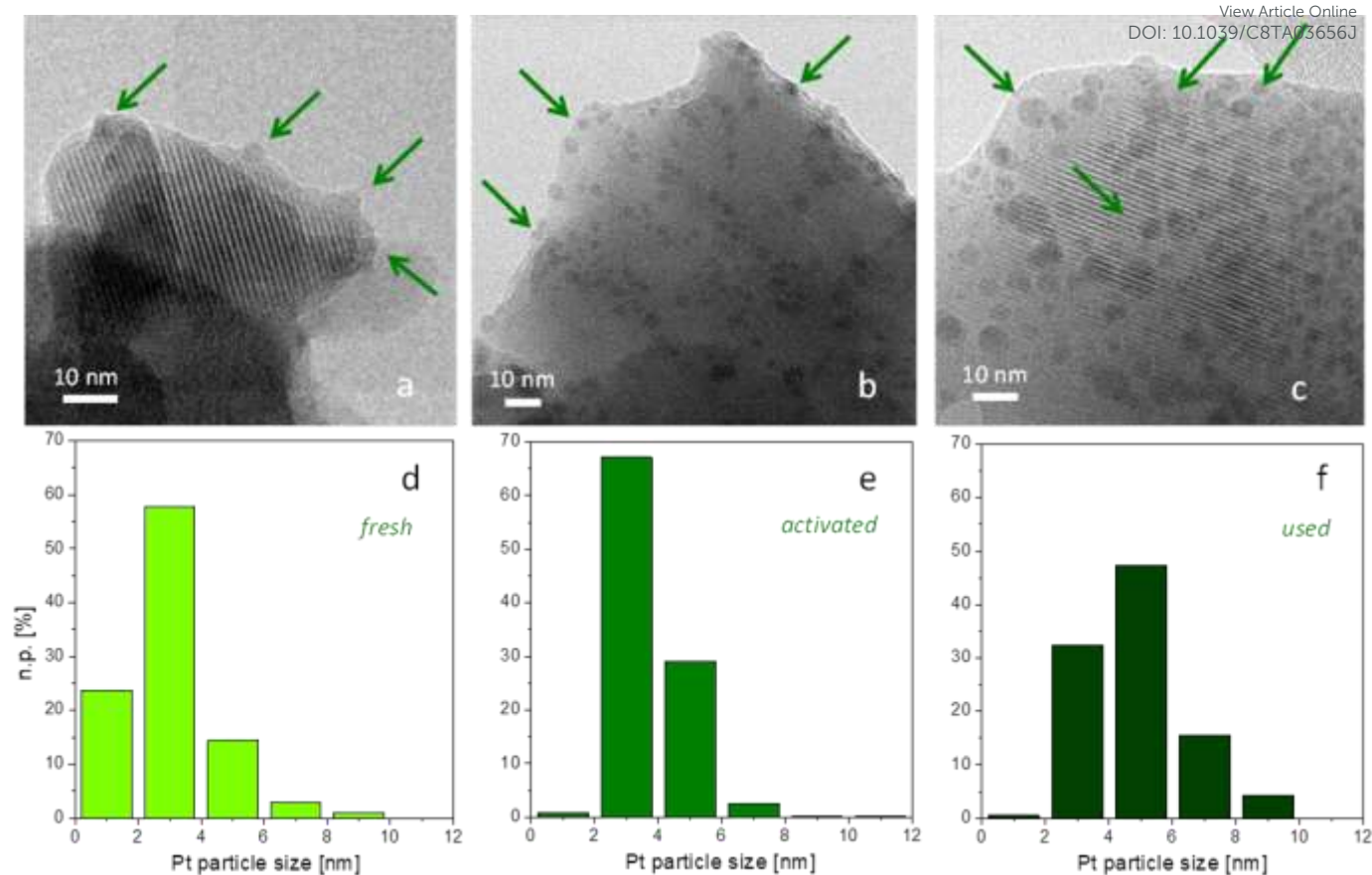


Fig. 7 HR-TEM images and Pt particle size distribution of the fresh (sections a and d, respectively), activated (sections b and e, respectively) and used (sections c and f, respectively) 3 wt. % Pt/CuCl catalyst. The Pt NPs are highlighted by green arrows. Instrumental magnification: 150000 \times .

The comparison between the particle size distributions reported in sections c and d of Figure 8 revealed restrained agglomeration of the Pt NPs (from 3.6 ± 2.0 nm to 4.2 ± 2.2 nm) during the catalysis. As for the high metal loading catalyst (7 wt%), Pt NP size distributions (for both the activated and post-catalysis samples) are broader than those obtained for the 3 wt% Pt/CuCl catalyst with modest metal loading. However, a large fraction of the Pt NPs are around 3 nm (Figures 8 a and b) and the average sizes are almost identical, ruling out the possible influence of particle size on the ensuing catalysis. This further vindicates the benefits of the design approach for the controlled formation of uniformly distributed metal nanoparticles and highlights the advantages of site isolation, in the samples with modest metal loadings, for achieving superior catalytic turnovers. In accordance with our observations on the 3 wt% Pt/CuCl catalyst, the high loading 7 wt% Pt sample retains its crystallinity and structural integrity post-activation and during catalysis. Based on the particle size distributions obtained by TEM

and HR-TEM analyses, the metal SSA was also calculated for both 3 wt% Pt (fresh, activated and used samples) and 7 wt% Pt (activated and used) catalysts in order to disclose the effect of the activation and use. The Pt average size and SSA are contrasted in Table 2.

Table 2 Pt average size and metal SSA obtained for the 3 wt. % and 7 wt% Pt/CuCl catalysts.

3 wt% Pt CuCl catalyst		
Pretreatment	Pt average size (nm)	Pt SSA (m ² /g)
Fresh	2.8 ± 1.4	30.7
Activated	3.6 ± 1.1	31.4
After catalysis	4.8 ± 1.7	23.7
7 wt% Pt CuCl catalyst		
Pretreatment	Pt average size (nm)	Pt SSA (m ² /g)
Activated	3.6 ± 2.0	20.3
After catalysis	4.2 ± 2.2	20.6

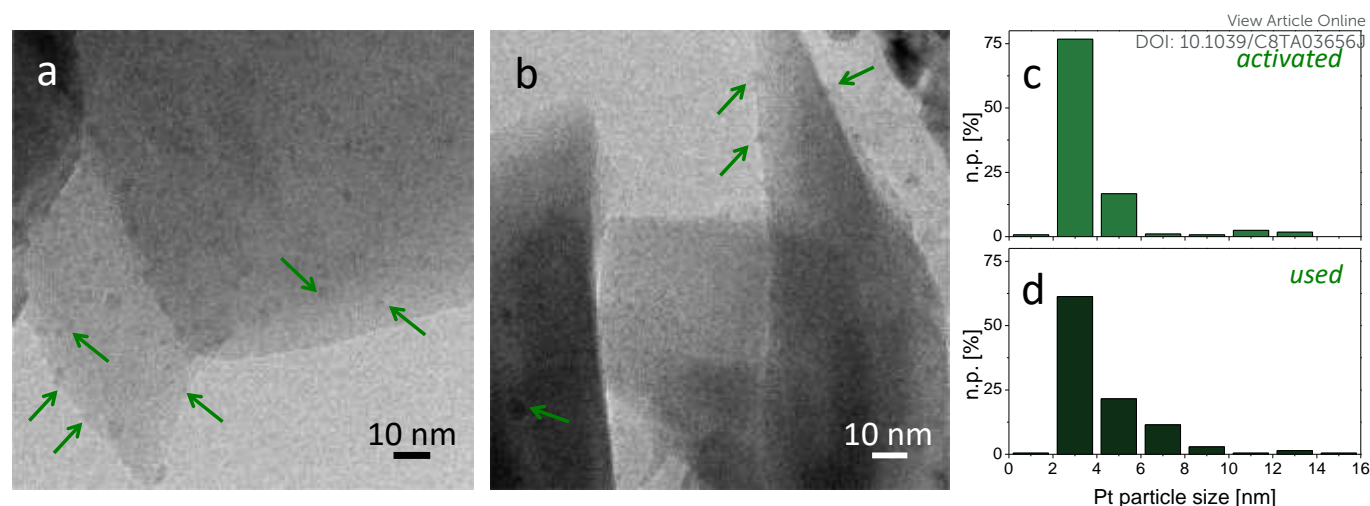


Fig. 8 HR-TEM images and Pt particle size distribution of the activated (sections a and c, respectively), and used (sections b and d, respectively) 7 wt. % Pt/CuClP catalyst. The Pt NPs are highlighted by green arrows. Instrumental magnification: 150000 \times .

In the case of the modest metal loading 3 wt% Pt CuClP catalyst, the small increase of Pt average size occurring upon activation and after catalysis (discussed previously) is firstly accompanied by a small increase of the Pt SSA after activation and then by a contained decrease after reaction. With the 7 wt% Pt sample, the Pt SSA is maintained during catalysis, reasonably due to the presence of NPs with larger size, which scarcely contribute to the SSA.

These results indicate that, given the optimal Pt loading, the activation procedure efficiently facilitated the extrusion of Pt NPs with small size, but this was accompanied by small increase in the particle size during catalysis, which did not have an adverse effect of the catalytic performance with time-on-stream (as evidenced in Fig 6). Further, the analyses performed on the used catalysts point out a robust interaction with the framework during the catalytic tests in air flow, presumably arising from the extrusion procedure. Continuous-flow catalytic tests are more appealing (minimise NP leaching) from an industrial perspective, as with zeolite catalysts, as longer catalyst lifetimes can be envisaged compared to batch processes.

Conclusions

With the aim of optimising the design of a more efficient catalytic system for the aerobic oxidation of KA oil, Pt NPs extruded from a copper chloropyrophosphate framework have been synthesized with low (1 wt %), optimal (3 wt %) and high (5 and 7 wt %) metal (Pt) loadings. Pt/CuClP material with low loadings, as well as the blank CuClP framework, showed no catalytic activity and a decreased turnover efficiency was noted with the catalysts with high Pt loadings.

A optimal loading of Pt was required to achieve high TONs (924) and a clear dependence on site isolation was observed, with high metal loadings leading to inferior turnover numbers (654 and 514, respectively for the 5 and 7 wt. % Pt/CuClP catalysts). A direct correlation between the catalytic activity (TOF), the degree of extrusion and extent of site isolation has been proposed, where optimal metal loadings are crucial for improved extrusion efficiency and increased catalytic turnovers.

By deploying a combined X-ray diffraction and Diffuse Reflectance UV-Vis-NIR spectroscopy approach, the incorporation of $[\text{PtCl}_4]^{2-}$

anions that leads to the generation of highly active Pt NP catalysts supported on the 1D copper chloropyrophosphate (CuClP) framework was monitored, both during activation and catalysis.

Our findings further highlight that the extrusion process is critically linked to the Pt content and therefore activation conditions need to be optimised, depending on the metal loading. The extrusion capability of the fresh catalysts depend directly on the amount of the $[\text{PtCl}_4]^{2-}$ anions included in the 1D channels, which in turn is contingent on the metallic precursor loaded during the synthesis. Based on these results, the prevalence of complete extrusion (post activation) was noted for catalysts with modest and high Pt loadings, in agreement with the PXRD and catalytic results. With low loadings (1 wt % Pt), a more effective activation procedure is required to remove $[\text{CuCl}_4]^{2-}$ ions within the 1D channels, which hinder the extrusion of the $[\text{PtCl}_4]^{2-}$ moieties.

The catalytic oxidation of KA oil, under continuous flow conditions, was also investigated for the first time through the deployment of combined spectroscopic tools. *In situ* FTIR has proven to be a powerful spectroscopic tool for monitoring the catalytic reaction, yielding unique insights into the nature of the species adsorbed on the catalyst surface, both during and after catalysis. In addition, the HR-TEM results revealed the presence of homogeneous and highly dispersed Pt nanoparticles, indicating robust nanoparticle and host framework structural stability, post catalysis.

Combined with our previous knowledge,³⁶⁻³⁹ these results represent a significant step in the further refinement and development of these nanoparticle catalysts, as new insights into the optimal loading and extrusion efficiency can help tailor uniformly-distributed metal nanoparticles for achieving superior catalytic turnovers.

Conflicts of interest

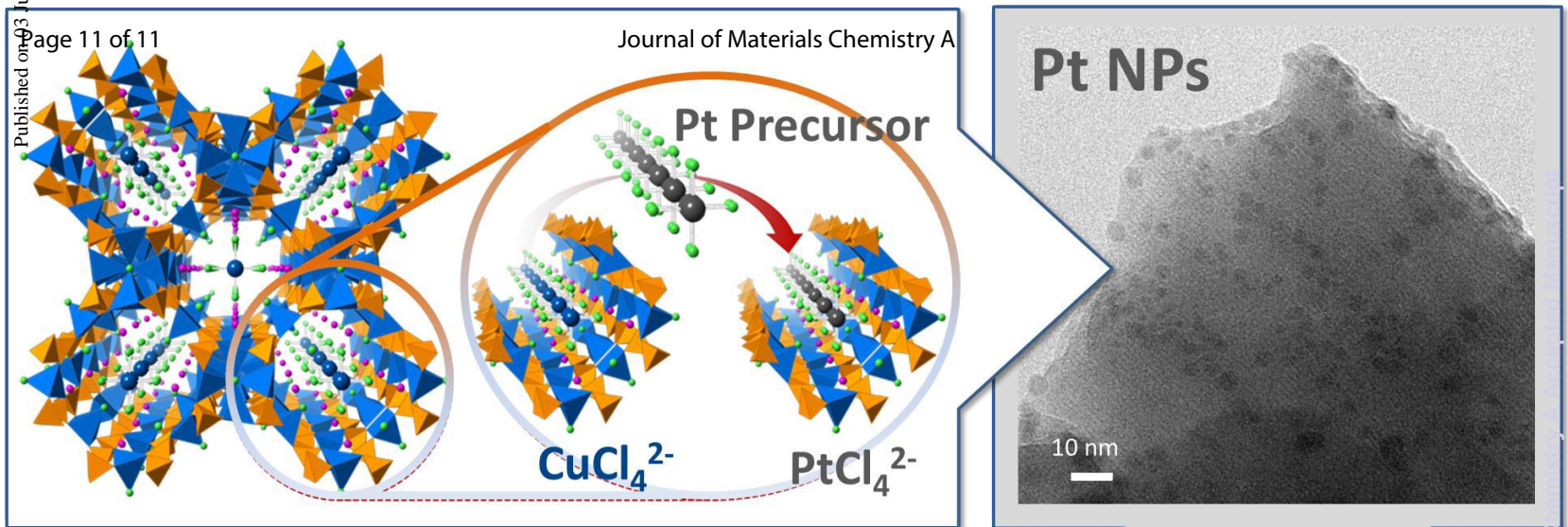
There are no conflicts to declare.

Acknowledgements

M. Manzoli and G. Cravotto are grateful for financial support from the University of Turin (Ricerca Locale 2016 - 2017).

References

- W. B. Fisher and J. F. Van Peppen, in Kirk-Othmer Encyclopaedia of Chemical Technology, Cyclohexanol and Cyclohexanone, 2005, pp. 1-7.
- M. T. Musser, in Ullmans Encyclopaedia of Industrial Chemistry, Cyclohexanol and Cyclohexanone, 200, pp. 49-60.
- United States Patent, US4918239, 1990.
- J. M. Thomas and R. Raja, *Proc. Natl. Acad. Sci. U. S. A.*, 2005, **102**, 13732.
- United States Patent, US7579506, 2009.
- United States Patent, US5395976, 1995.
- Japanese Patent, WO2014163080A1, 2014.
- United States Patent Office, US2338445, 1944.
- United States Patent, US7579506, 2009.
- R. Ciriminna, E. Falletta, C. Della Pina, J.H. Teles and M. Pagliaro., *Angew. Chemie. Int. Ed.*, 2016, **55**, 14210.
- G. Bai, H. Wang, H. Ning, F. He, G. Chen, *React Kinet Catal Lett*, 2008, **94**, 375.
- D. Ji, W. Zhu, Z. Wang and G. Wang, *Catal. Commun.*, 2007, **8**, 1891.
- B.M. Reddy, K. J. Ratnam and P. Saikia, *J. Mol. Catal. A.*, 2006, **252**, 238.
- G. Ranga Rao, S. Kumar Meher, B. G. Mishra, P. Hari and K. Charan, *Catal Today*, 2012, **198**, 140.
- J. Ni, W.-J. Yu, L. He, H. Sun, Y. Cao, H.-Y. He and K.-N. Fan, *Green Chem.*, 2009, **11**, 756.
- V. Mahdavi and S. Soleimani, *Mater. Res. Bull.*, 2014, **51**, 153.
- M. Alizadeh, F. Farzaneh and M. Ghandi, *J. Mol. Catal. A.*, 2003, **194**, 283.
- M. L. Parentis, N. A. Bonini and E. E. Gonzo, *Reaction Kinetics and Catalysis Letters*, 2002, **76**, 243.
- B.-Z. Zhan, M. A. White, T.-K. Sham, J. A. Pincock, R. J. Doucet, K. V. Ramana Rao, K. N. Robertson and T. S. Cameron, *JACS*, 2003, **125**, 2195.
- Y. Hong, X. Yan, X. Liao, R. Li, S. Xu, L. Xiao and J. Fan, *Chem. Commun.*, 2014, **50**, 9679.
- X. Huang, X. Wang, M. Tan, X. Zou, W. Ding and X. Lu, *App. Catal. A.*, 2013, **467**, 407.
- G. Zhao, H. Hu, M. Deng, M. Ling and Y. Lu, *Green Chem.*, 2011, **13**, 55.
- K. Yamaguchi and N. Mizuno, *New J. Chem.*, 2002, **26**, 972.
- H. Wang, W. Kong, W. Zhu, L. Wang, S. Yang and F. Liu, *Catal. Commun.*, 2014, **50**, 87.
- A. Gavriilidis, A. Constantinou, K. Hellgardt, K. K. Hii, G. J. Hutchings, G. L. Brett, S. Kuhn and S. P. Marsden, *React. Chem. Eng.*, 2016, **1**, 595.
- B. Zhou, S. Han, R. Raja and G. A. Somorjai, *Nanotechnology in Catalysis*, Springer Science + Business Media, 2007, **3**.
- J. M. Thomas, R. Raja, G. Sankar and R. G. Bell, *Nature*, 1999, **398**, 227.
- R. Raja, G. Sankar and J. M. Thomas, *J. Am. Chem. Soc.*, 1999, **121**, 11926.
- J. M. Thomas and R. Raja, *Proc. Natl. Acad. Sci. U. S. A.*, 2005, **102**, 13732.
- J. M. Thomas, R. Raja and D. W. Lewis, *Angew. Chemie - Int. Ed.*, 2005, **44**, 6456.
- E. Ghedini, F. Menegazzo, M. Signoretto, M. Manzoli, F. Pinna, G. Strukul, *J. Catal.*, 2010, **273**, 266.
- J. A. Armstrong, E. R. Williams and M. T. Weller, *J. Am. Chem. Soc.*, 2011, **133**, 8252.
- E. R. Williams, S. A Morris and M. T. Weller, *Dalton Trans.*, 2012, **3**, 10845.
- J. Rouse, K. V Redrup, E. Kotsapa and M. T. Weller, *Chem. Commun.*, 2009, **46**, 7209. DOI: 10.1039/C8TA03656J
- E. R. Williams, R. M. Leithall, R. Raja and M. T. Weller, *Chem. Commun*, 2013, **49**, 249.
- C. S., Hinde, S. Van Aswegen, G. Collins, J.D. Holmes, T.S. Hor, R. Raja, *Dalton Trans.* **2013**, 42, 12600.
- C. S. Hinde, A. M. Gill, P. P. Wells, T. S. A. Hor and R. Raja, *ChemPlusChem*. 2015, **80**, 1226.
- C. S. Hinde, D. Ansovini, P. P. Wells, G. Collins, S. Van Aswegen, J. D. Holmes and R. Raja, *ACS Catal.* **2015**, 5, 3807.
- A. M. Gill, C. S. Hinde, R. K. Leary, M. E. Potter, A. Jouve, P. P. Wells, P. A. Midgley, J. M. Thomas and R. Raja, *ChemSusChem*, 2016, **9**, 423.
- United States Patent US 62235684, 2015.
- C. Amuli, M. Elleb, J. Meullemeestre, M. Schwing and F. Vierling, *Inorg. Chem.*, 1986, **25**, 856.
- W.L. Waltz, J. Lilie, A. Goursot and H. Chermette, *Inorg. Chem.*, 1989, **28**, 2247.
- E. V Kondratenko, Y. Sakamoto, K. Okumura and H. Shinjoh, *Catal. Today*, 2011, **164**, 46.
- L. Kesavan, R. Tiruvalam, M.H.A. Rahim, M. I. bin Saiman, D. I. Enache, R.L. Jenkins, N. Dimitratos, J.A. Lopez-Sanchez, S.H. Taylor, D. W. Knight, C. J. Kiely and G.J. Hutchings, *Science*, 2011, **331**, 195.



Decreasing Pt Metal Loading

Better Extrusion Efficiency

Increasing Catalytic Turnover